



Three-dimensional Global Hybrid Simulation of Magnetosheath Jets at Mercury

Jin Guo^{1,2} , San Lu^{1,2,3} , Quanming Lu^{1,2,3} , Junyi Ren^{1,2} , Jiuqi Ma^{1,2} , James A. Slavin⁴ , Weijie Sun⁵ ,
Jun Zhong⁶ , Xinliang Gao^{1,2,3} , Rajkumar Hajra^{1,2}, and Rongsheng Wang^{1,2,3}

¹ School of Earth and Space Sciences/Deep Space exploration Laboratory, University of Science and Technology of China, Hefei, People's Republic of China; lusan@ustc.edu.cn; qmlu@ustc.edu.cn

² CAS Center for Excellence in Comparative Planetology/CAS Key Lab of Geospace Environment, University of Science and Technology of China, Hefei, People's Republic of China

³ Collaborative Innovation Center of Astronautical Science and Technology, Harbin, People's Republic of China

⁴ Department of Climate and Space Sciences and Engineering, University of Michigan, Ann Arbor, MI, USA

⁵ Space Science Laboratory, University of California, Berkeley, CA, USA

⁶ Key Laboratory of Earth and Planetary Physics, Institute of Geology and Geophysics, Chinese Academy of Sciences, Beijing, People's Republic of China
Received 2024 November 13; revised 2024 December 10; accepted 2024 December 11; published 2024 December 27

Abstract

Plasma high-speed jets are common in Earth's magnetosheath, and they significantly perturb the magnetosheath and affect the magnetosphere. The space environment of Mercury, characterized by the bow shock, magnetosheath, and magnetosphere, shares many similarities with that of Earth, so high-speed jets may also be formed in Mercury's magnetosheath. Here we examine the formation of magnetosheath jets using a three-dimensional global hybrid simulation. The simulation results demonstrate that magnetosheath jets may be formed by the passage of upstream compressive structures through the bow shock. The number and size of the jets are significantly smaller than those at Earth because of Mercury's smaller magnetosphere size. Under the impact of magnetosheath jets, Mercury's magnetopause undergoes significant deformation up to $0.19 R_M$ (R_M is Mercury's radius). These simulation results are expected to be tested by the BepiColombo mission.

Unified Astronomy Thesaurus concepts: Mercury (planet) (1024); Planetary bow shocks (1246); Planetary magnetospheres (997); Solar-planetary interactions (1472); Planetary boundary layers (1245)

1. Introduction

Magnetosheath jets, also known as high-speed jets, are structures with large dynamic pressure commonly observed in Earth's magnetosheath downstream of the quasi-parallel bow shock (e.g., Z. Němeček et al. 1998; H. Hietala et al. 2009). The plasma flows within these jets are often directed toward Earth and exceed the local Alfvén speed (F. Plaschke et al. 2013). The characteristic spatial size of magnetosheath jets parallel to the propagation direction is about $0.15 R_E$ (R_E is Earth's radius; F. Plaschke et al. 2020), with some large jets reaching several R_E (H. Hietala et al. 2012; H. Gunell et al. 2014; Y. Hao et al. 2016; Y. Omelchenko et al. 2021). The recurrence time of magnetosheath jets is of the order of several minutes (F. Plaschke et al. 2013). J. Guo et al. (2022a) suggested that large and geoeffective magnetosheath jets are more likely to form when the interplanetary magnetic field (IMF) aligns with the solar wind velocity. Some well-known formation mechanisms of magnetosheath jets have been proposed, including shock reformation (S. Raptis et al. 2022) and the interaction of compressive structures (CSs; T. Karlsson et al. 2015; J. Suni et al. 2021; J. Ren et al. 2023) with the quasi-parallel bow shock. When the magnetosheath jets impact the magnetopause, they can trigger magnetic reconnection at the magnetopause (H. Hietala et al. 2018; Y. Omelchenko et al. 2021), excite surface waves on the magnetopause (M. Archer et al. 2019) or compressive waves in the magnetosphere (F. Plaschke et al. 2009), trigger impulsive plasma penetration (H. Gunell et al. 2012; A. Dmitriev & A. Suvorova 2015), and

even trigger dayside auroras in the ionosphere (D. S. Han et al. 2017). Using three-dimensional (3D) global hybrid simulations, J. Ren et al. (2024) suggested that the magnetosheath jets surround the magnetosheath cavities, resulting in an overall 3D honeycomb-like magnetosheath structure. Magnetosheath cavities are structures with high-energy particles and low dynamic pressure within Earth's magnetosheath, where the plasma flow velocity, density, and magnetic field are all reduced (e.g., F. Katırcıoğlu et al. 2009). Honeycomb-like magnetosheath structure is a combination of magnetosheath jets and cavities, which may potentially cause turbulence in the magnetosheath and global deformation of the magnetopause. Similar findings were also reported subsequently by S. Fatemi et al. (2024) using 3D global hybrid simulations. Recent studies found that jets are also formed in Jovian magnetosheath (Y. Zhou et al. 2024), Martian magnetosheath (H. Gunell et al. 2023), and even magnetosheath downstream of interplanetary shocks (H. Hietala et al. 2024), but they have yet to be directly observed in Mercury's magnetosheath due to the limited plasma measurements of previous spacecraft.

The space environment of Mercury, such as the bow shock, magnetosheath, and magnetosphere, shares many similarities with Earth's, but there are also many differences (J. A. Slavin et al. 2008; J. Slavin et al. 2019; J. Zhong et al. 2020; W. Sun et al. 2022). Magnetic field observations from the MERcury Surface, Space ENvironment, GEOchemistry, and Ranging mission revealed that Mercury possesses an intrinsic magnetic field with the magnetic field strength near planetary equator of about 195 nT, which is only one-hundredth that of Earth (B. J. Anderson et al. 2011). This weak intrinsic magnetic field interacts with the solar wind to form a small magnetosphere and bow shock. The typical bow shock and magnetopause standoff distances are about 1.96 and 1.45 R_M (R_M is Mercury's radius) from the center of the

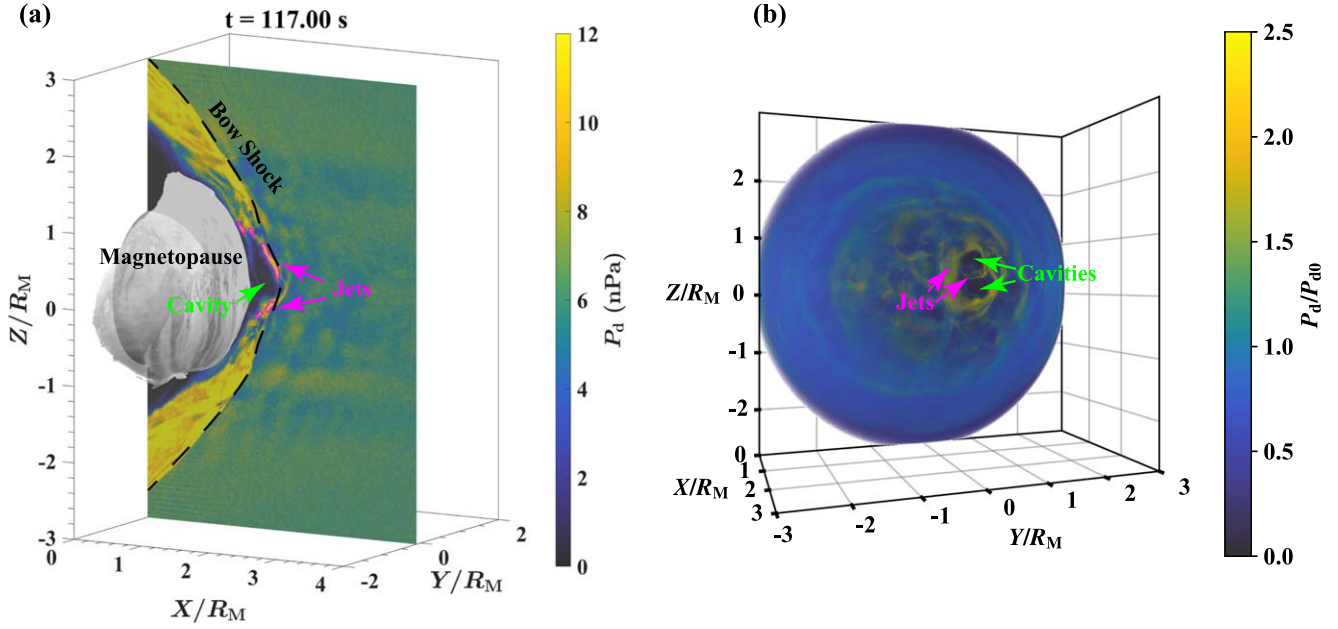


Figure 1. Plasma jets and cavities in Mercury’s magnetosheath under a radial IMF at $t = 117$ s. (a) Dynamic pressure (P_d) near the noon–midnight meridian plane. The gray 3D surface, identified by the boundary of the open–closed field lines, represents the magnetopause. The black dashed line indicates the bow shock, and the violet contour indicates P_d that is two times the background dynamic pressure (P_{d0}) in the magnetosheath. P_{d0} is obtained by smoothing the magnetosheath dynamic pressure with a 3D window of $0.21 R_M \times 0.21 R_M \times 0.21 R_M$. (b) The ratio of P_d and P_{d0} downstream of the bow shock.

magnetic dipole, respectively (R. M. Winslow et al. 2013). The solar wind around Mercury has an Alfvénic Mach number of about 2–5 (J. A. Slavin & R. E. Holzer 1981; C. Russell et al. 1982; M. Sarantos & J. A. Slavin 2009; W. Sun et al. 2022), which is lower than the typical value of about 7–10 around Earth (E. Marsch et al. 1982). Many studies have revealed shock-related structures and waves similar to those at Earth, such as shock reformation (T. Sundberg et al. 2013), isolated magnetic field structures in the magnetosheath (T. Karlsson et al. 2016), electromagnetic ion cyclotron waves in the magnetosheath (T. Sundberg et al. 2015), and ultralow frequency waves in the foreshock (N. Romanelli et al. 2020; N. Romanelli & G. DiBraccio 2021; Y. Wang et al. 2023). Although Mercury’s bow shock and magnetosheath are similar to Earth’s, the low Alfvén Mach number and Mercury’s smaller magnetosheath raise the question of whether magnetosheath jets can form at Mercury. Moreover, it is worth exploring whether Mercury’s small magnetosphere can enable the formation of honeycomb-like magnetosheath structures. Although various global simulation models have been applied to study Mercury’s magnetospheric system and the bow shock (H. Egan et al. 2019; X. Jia et al. 2019; S. Fatemi et al. 2020; G. Lapenta et al. 2022; Q. Lu et al. 2022; Z. Shi et al. 2022; J. Guo et al. 2023a; C. Li et al. 2024), the magnetosheath jets have not been simulated.

In this study, we explore whether the magnetosheath jets can form at Mercury using a 3D global hybrid simulation model. Our simulation results suggest that magnetosheath jets, commonly observed at Earth, may also form at Mercury and are the results of upstream CSs. This hypothesis may be tested by the observational data from the BepiColombo spacecraft, which will be orbiting Mercury in 2027.

2. Simulation Model

A 3D global hybrid code named as gcPIC-hybrid is used to simulate the magnetosheath jets at Mercury. In hybrid simulations, ions are treated as particles and electrons as a massless fluid,

assuming quasi-charge neutrality. The gcPIC is a software package, including full particle and hybrid simulation within a general curvilinear coordinate system. This software package has been previously employed to study the excitation of chorus waves in a dipole magnetic field (Q. Lu et al. 2019), the evolution of flux transfer events at Earth (J. Guo et al. 2021a, 2021b, 2022b, 2023b), and the disappearing dayside magnetosphere at Mercury (J. Guo et al. 2023a). The details of the model are described in J. Guo et al. (2023a), and here only a brief introduction is described. The hybrid simulation model adopts the Mercury Solar Orbital coordinate system. The simulation domain spans $-3 R_M \leq x \leq 5 R_M$, $-4 R_M \leq y \leq 4 R_M$, and $-5 R_M \leq z \leq 5 R_M$, utilizing Cartesian coordinates for calculations. Mercury’s dipole moment is set to $195 \text{ nT} \cdot R_M^3$ along the z -direction, with a $0.2 R_M$ offset northward from the planetary center (e.g., B. J. Anderson et al. 2011). The ion kinetic physics can be well resolved with grid sizes comparable to local ion inertial length, and a nonuniform grid cell system is employed accordingly, with a grid size of $\Delta x = \Delta y = \Delta z = 0.009 R_M$ (equal to the ion inertial length in the magnetosheath) in the near-Mercury regions. The number of grids is $N_x \times N_y \times N_z = 643 \times 550 \times 602$, and each grid in the magnetosheath contains at least 80 particles.

The solar wind conditions in the simulation are derived from typical observation values (W. Sun et al. 2022). The solar wind speed is 350 km s^{-1} along the $-x$ -direction; the plasma density in the solar wind is 30 cm^{-3} ; the solar wind dynamic pressure is 6.1 nPa ; the IMF is $(B_{\text{sw},x}, B_{\text{sw},y}, B_{\text{sw},z}) = (25, 0, 0) \text{ nT}$, which is beneficial for large-scale jets formation (F. Plaschke et al. 2013; J. Guo et al. 2022a; J. Ren et al. 2023); the Alfvénic Mach number, defined as the ratio between the solar wind speed and the Alfvén speed, is 3.5; the β of solar wind plasma, which is the ratio of the plasma pressure to the magnetic pressure, is $\beta_i = \beta_e = 0.29$. The time step Δt is chosen as $0.01 \Omega_i^{-1}$, where Ω_i is the ion gyrofrequency based on the IMF intensity.

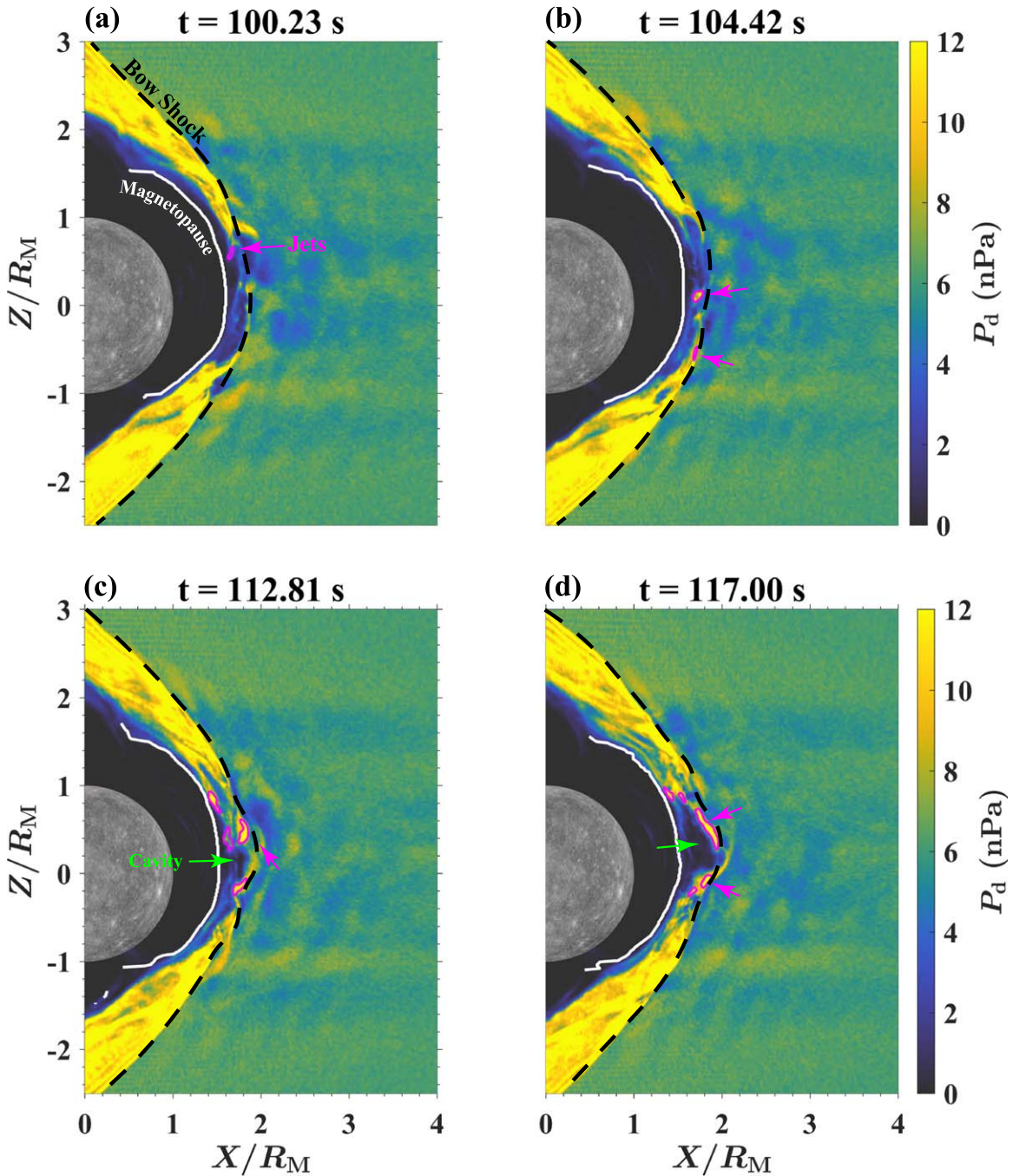


Figure 2. Magnetosheath jets downstream of the bow shock near the meridian plane at $t = 100.23$, 104.42 , 112.81 , and 117.00 s under a radial IMF. The white lines and black dashed lines indicate the magnetopause and the bow shock, respectively.

3. Simulation Results

3.1. Magnetosheath Jets' Structure

Figure 1 shows a 3D overview of magnetosheath jets and magnetosheath cavities at $t = 117.00$ s under a radial IMF. Since the IMF is radial, the bow shock is quasi-parallel and rippled near the subsolar region and quasi-perpendicular near the flank region. The magnetopause, magnetosheath, and bow shock are all shifted northward because of the northward offset of the internal dipole. The standoff distances of the magnetopause and the bow shock near the subsolar region are about 1.5 and $2.0 R_M$, respectively, and the magnetosheath thickness is about $0.5 R_M$ between them.

In Figure 1(a), downstream of the quasi-parallel shock, there are two magnetosheath jets with enhanced dynamic pressure (P_d). The jet boundary is defined where the P_d is twice the background dynamic pressure (P_{d0}) in the magnetosheath (M. Archer & T. Horbury 2013; J. Guo et al. 2022a). Adjacent to the jets is the magnetosheath cavity, characterized by the reduced P_d . Figure 1(b) illustrates the ratio of P_d and P_{d0} downstream of the bow shock, showing the 3D structure of magnetosheath jets and cavities. Regions where the value of P_d/P_{d0} exceeds 2 are identified as the magnetosheath jets. It is found that magnetosheath jets surround the quasi-circular cavities. There are only two obvious jet-surrounded cavities due to Mercury's small magnetosheath. Therefore, honeycomb-like

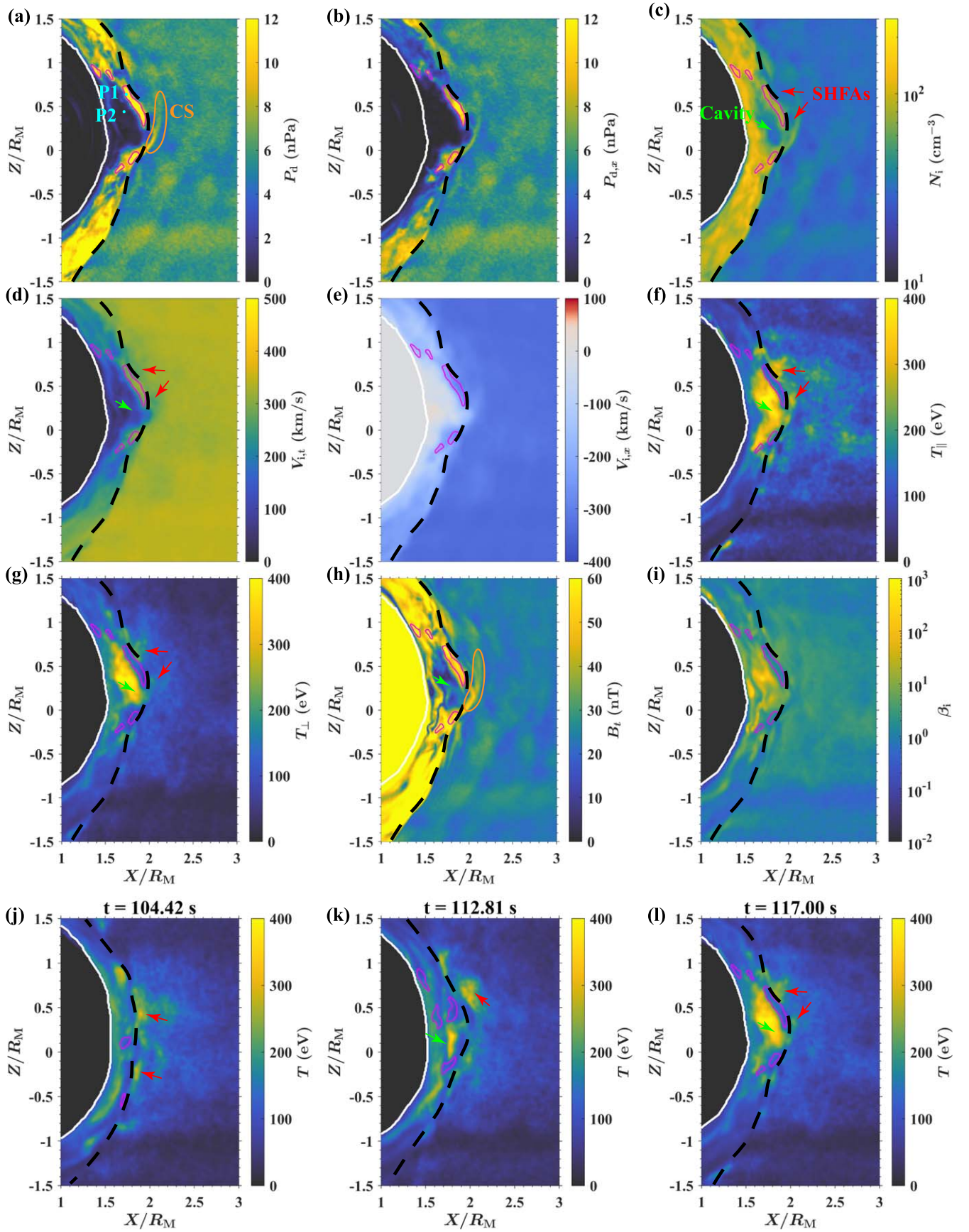


Figure 3. Characteristics of magnetosheath jets, cavities, upstream CSs, and SHFAs at $t = 117.00$ s. (a) Dynamic pressure (P_d), (b) dynamic pressure in x -direction ($P_{d,x}$), (c) ion density (N_i), (d) total ion velocity (V_i), (e) ion velocity x -component ($V_{i,x}$), (f) ion parallel temperature (T_{\parallel}), (g) ion perpendicular temperature (T_{\perp}), (h) total magnetic field (B_t), (i) ion beta (β_i), and ion temperature (T) at $t = 104.42$ (j), 112.81 (k), and 117.00 s (l). The green and red arrows indicate the magnetosheath cavities and SHFAs, respectively. The orange circles indicate the CSs in panels (a) and (h). The points “P1” and “P2” marked in panel (a) are the positions of two virtual satellites.

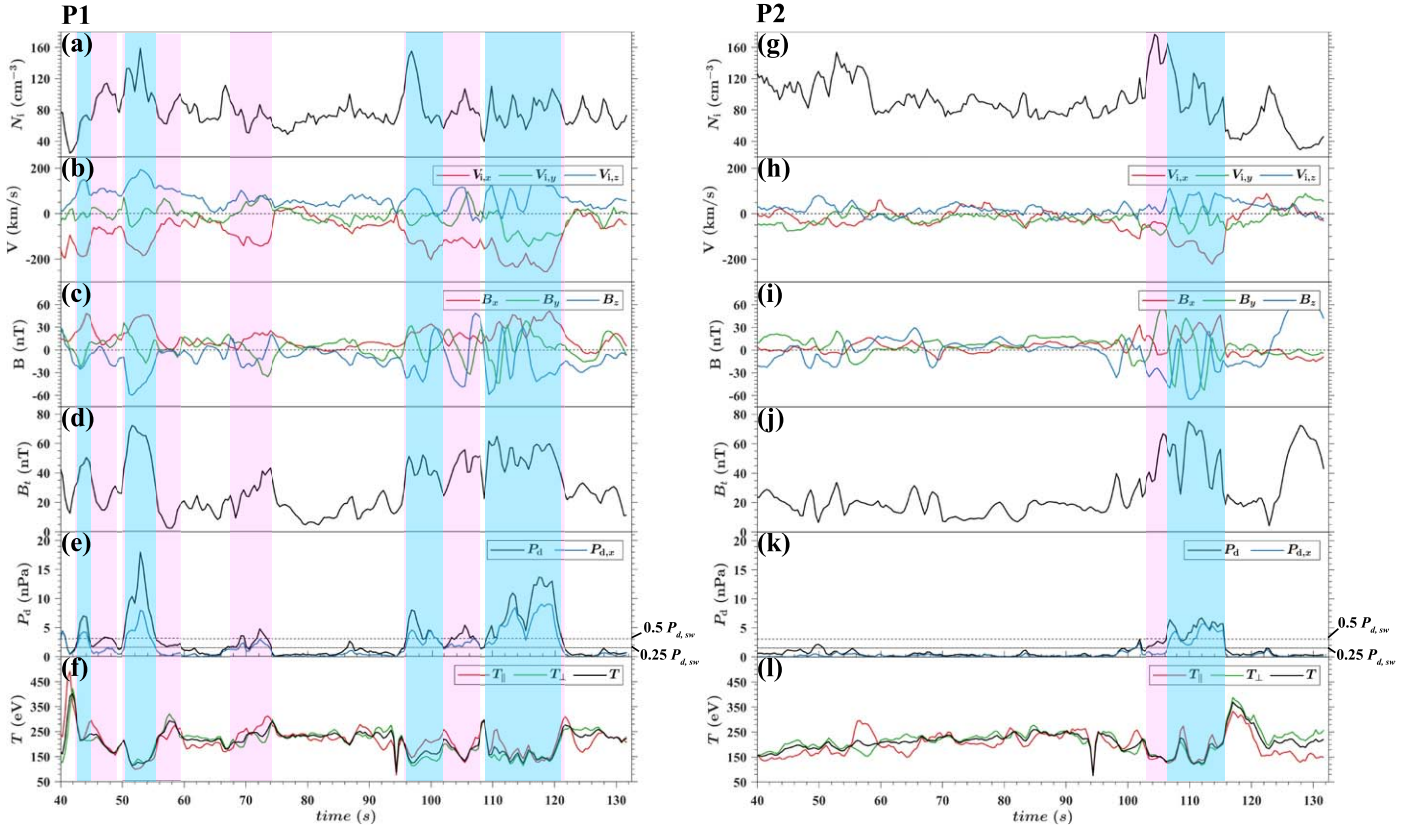


Figure 4. Plasma and magnetic field parameters observed by two virtual satellites in the magnetosheath. (a), (g) Ion density (N_i), (b), (h) ion velocity MSO components ($V_{i,x}$, $V_{i,y}$, and $V_{i,z}$), (c), (i) magnetic field MSO components (B_x , B_y , and B_z), (d), (j) total magnetic field (B_t), (e), (k) dynamic pressure (P_d) and dynamic pressure x -component ($P_{d,x}$), and (f), (l) ion temperature at points P1 = (1.75, -0.11, 0.67) R_M (left panels) and P2 = (1.71, -0.11, 0.46) R_M (right panels). These two points are indicated in Figure 3(a). The blue-shaded (blue- and magenta-shaded) regions indicate the magnetosheath jet intervals, which are identified as the period when $P_{d,x} > 0.25 P_{d,sw}$ ($P_d > 0.25 P_{d,sw}$). The dotted and dashed lines in panels (e) and (k) indicate $0.5 P_{d,sw}$ and $0.25 P_{d,sw}$, respectively.

magnetosheath structures, which form in Earth’s magnetosheath (J. Ren et al. 2024), are not formed at Mercury in this simulation.

Figure 2 shows P_d near the noon–midnight meridian plane at different times. The interval from $t = 100.23$ to 117.00 s is selected to better present the evolution of magnetosheath structures. The jets have a parallel size ranging from 0.15 to $0.53 R_M$ and a perpendicular size about $0.1 R_M$. Some large-scale jets can traverse the magnetosheath and impact the magnetopause (Figures 2(b) and (d)). The diameter of magnetosheath cavities ranges approximately between 0.4 and $0.8 R_M$.

To clearly illustrate the detailed characteristics of magnetosheath jets, Figures 3(a)–(i) show various plasma and magnetic field parameters near the meridian plane at $t = 117.00$ s. In Figure 3(b), the x -component of dynamic pressure ($P_{d,x}$), which is commonly utilized in spacecraft observations for jet identification (F. Plaschke et al. 2013; Raptis et al. 2020), is enhanced in the magnetosheath jets. Plasma density (N_i) and magnetic field (B_t) are also enhanced within the magnetosheath jets (Figures 3(c) and (h)). Since the plasma in the magnetosheath jets is less heated by the bow shock (e.g., H. Hietala et al. 2009; H. Karimabadi et al. 2014; M. Palmroth et al. 2018), the ion parallel and perpendicular temperatures (T_{\parallel} and T_{\perp}) are lower in the jets compared to the surroundings (Figures 3(f) and (g)). Previous studies have suggested that there are generally sunward flows around Earth’s magnetosheath jets (J. H. Shue et al. 2009; F. Plaschke et al. 2017; J. Guo et al. 2022a; S. Fatemi et al. 2024). However, in Figure 3(e), there are no sunward flows around

Mercury’s magnetosheath jets (as confirmed by ion velocity x -component, V_x). The upstream CSs have similar plasma and magnetic field properties to the magnetosheath jets, including enhanced P_d and B_t (Figures 3(a) and (h)), as well as lower ion temperature (Figures 3(f) and (g)) compared to the surroundings. Similar to jets in Earth’s magnetosheath, these magnetosheath jets are formed by the upstream CSs (M. Palmroth et al. 2018; J. Suni et al. 2021; J. Ren et al. 2023). Spontaneous hot flow anomalies (SHFAs) are also found upstream of the quasi-parallel bow shock (Figure 3). Conversely, the magnetosheath cavities and upstream SHFAs have opposite properties to the magnetosheath jets. In the magnetosheath cavities and upstream SHFAs, P_d , N_i , total ion velocity (V_t), and B_t decrease, while the ion temperature increases relative to the surroundings (Figures 3(a)–(d) and (f)–(h)). Global hybrid simulations performed by N. Omid et al. (2016) have shown that a magnetosheath cavity is formed by multiple SHFAs passing through the bow shock, explaining their similar properties.

Figures 3(j)–(l) show the ion temperature (T) near the meridian plane at $t = 104.42$, 112.81 , and 117.00 s. The upstream SHFAs continue moving toward the bow shock and passing through it, resulting in enlargement of the magnetosheath cavities, with hot plasma in the cavities extending to the north and south cusp regions by $t = 117.00$ s (Figure 3(l)). This may facilitate the precipitation of high-energy particles into Mercury’s magnetospheric cusps. The high ion temperature and low magnetic field result in high ion beta ($\beta_i \gg 1$) (Figure 3(i)) in the magnetosheath cavity.

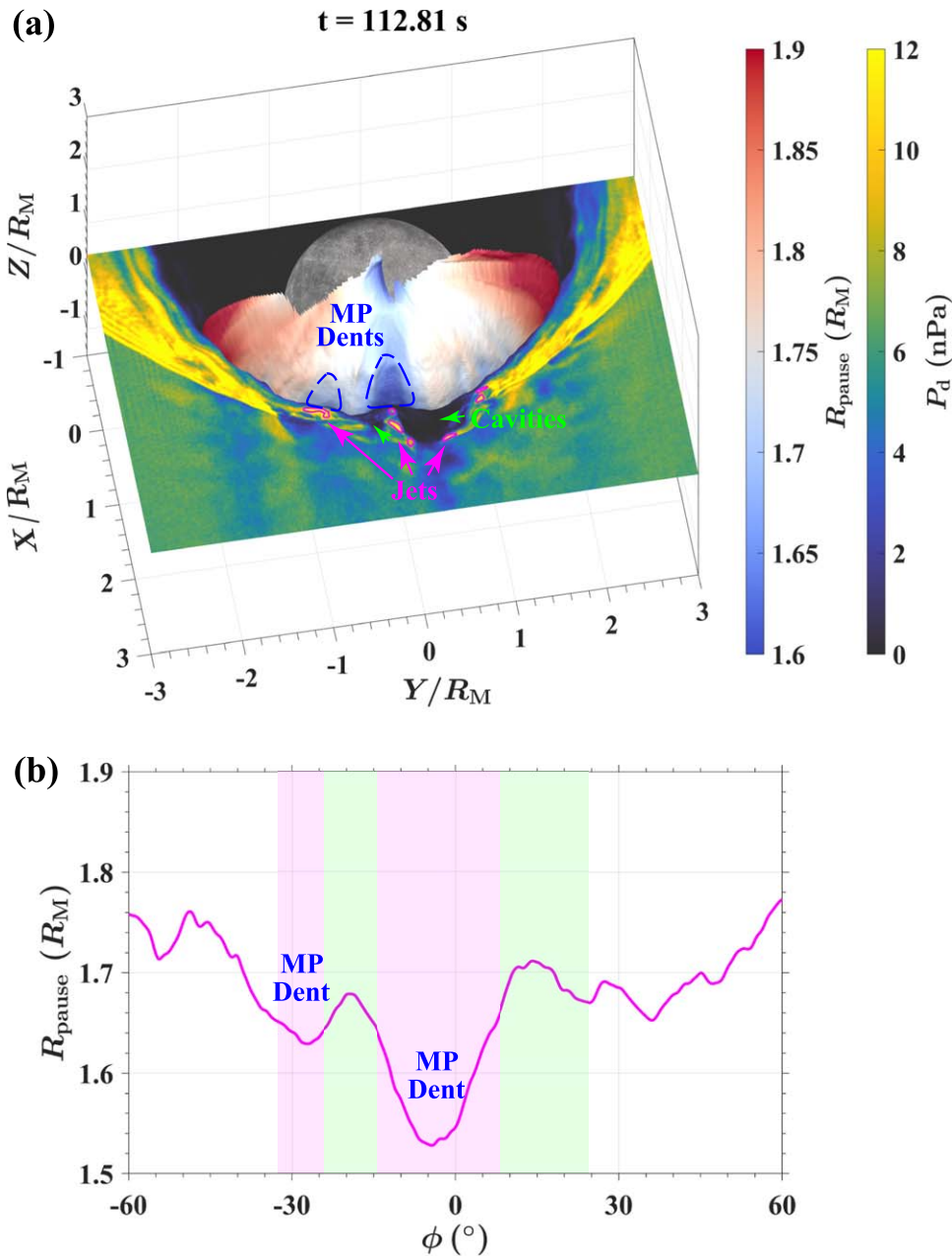


Figure 5. Magnetopause dent formed by the magnetosheath jets at $t = 112.81$ s. (a) P_d in the plane $z = 0.4 R_M$ and distance from the center of Mercury to the magnetopause (R_{pause}) at the magnetopause surface. The blue dashed circles indicate the magnetopause dent. (b) R_{pause} at different azimuthal angles (ϕ). $\phi = 0$ is along the x -direction. The magenta-shaded and green-shaded regions indicate the ϕ intervals of the magnetosheath jets and cavity, respectively.

3.2. Virtual Stationary Spacecraft Observations

To further investigate the magnetosheath jets at Mercury and emulating spacecraft observations, two virtual stationary spacecraft are placed in the simulation at different locations within the magnetosheath (Figure 3(a)). The first virtual stationary spacecraft is located at $P1 = (1.75, -0.11, 0.67)R_M$, where many magnetosheath jets pass through, and the second one is located at $P2 = (1.71, -0.11, 0.46)R_M$, predominantly in the magnetosheath cavities. The temporal evolutions of various plasma and magnetic field parameters observed by two virtual spacecraft are shown in Figure 4. In this section, we apply a criterion commonly used in spacecraft observations (e.g., F. Plaschke et al. 2013; S. Raptis et al. 2022) to identify the magnetosheath jets. In the magnetosheath jets, the maximum $P_{d,x}$ is required to exceed half

the solar wind dynamic pressure ($P_{d,sw}$). The jet time interval is defined as the period during which $P_{d,x} > 0.25 P_{d,sw}$. Since dynamic pressure in the flank regions of the magnetosheath is higher than that in the solar wind (Figure 1), we do not use the above criteria to identify jets in both 2D and 3D figures. Based on this criterion, four magnetosheath jets are identified at $P1$, and one at $P2$ from $t = 40$ to 130 s (indicated by the blue-shaded regions in Figure 4). However, many magnetosheath jets do not only flow along the x -direction (Figure 2), and the y and z components of dynamic pressure in the magnetosheath jets should also be considered. Therefore, we also use the total dynamic pressure (P_d) to identify the magnetosheath jets: the maximum $P_d > 0.5 P_{d,sw}$, and the jet interval is the period during which $P_d > 0.25 P_{d,sw}$ (magenta-shaded region in Figure 4). With this criterion, five

magnetosheath jets are identified at $P1$ within 90 s, and one is observed at $P2$. Note that the intervals of magnetosheath jets identified by the P_d criterion include those identified by the $P_{d,x}$ criterion. In these magnetosheath jets, N_i , B_t , and $V_{i,x}$ (i.e., the plasma flows toward the Mercury) are enhanced, while ion temperature is low (Figure 4). $V_{i,z}$ is also enhanced in some magnetosheath jets, indicating that these jets are deflected northward. If a spacecraft is located in a cavity, observing the jets becomes challenging, as seen with the virtual spacecraft at $P2$. Despite the low ion density in the cavities ($t = 118$ s, Figure 4(g)), the ions are fully heated by the bow shock, and the ion temperature is anisotropic (Figure 4(l)).

3.3. Magnetopause Dent Formed by Magnetosheath Jets

Previous studies have demonstrated that magnetosheath jets impact Earth's magnetopause, and they can dent the magnetopause (J. H. Shue et al. 2009; H. Hietala et al. 2012). The impact of magnetosheath jets on Mercury's magnetopause is investigated in Figure 5. Figure 5(a) shows the 3D magnetopause, colored by the distance from the dipolar center of Mercury to the magnetopause (R_{pause}), as well as the magnetosheath jets and cavities in the plane $z = 0.4 R_M$. The magnetosheath jets on the dawnside and near the meridian plane are close to the magnetopause and dent it significantly, while the duskside jets have little influence on it. A magnetosheath cavity surrounded by the jets is situated near the meridian plane. In the magnetosheath cavity, P_d is much lower, resulting in the magnetopause bulging outward. Figure 5(b) shows R_{pause} at different azimuthal angles (ϕ) in the plane $z = 0.4 R_M$ to quantify the deformation of the magnetopause. The magnetosheath jets on the dawnside and near the meridian plane dent the magnetopause in the interval of $-32^\circ < \phi < -24^\circ$ and $-15^\circ < \phi < 8^\circ$ (magenta-shaded regions in Figure 5(b)), respectively. At the magnetopause dent, R_{pause} can be as low as $1.52 R_M$. A large-scale magnetosheath cavity is located in interval of $8^\circ < \phi < 25^\circ$, where R_{pause} can reach up to $1.71 R_M$. Therefore, the deformation of the magnetopause can be up to $0.19 R_M$, accounting for about 13% of the magnetopause standoff distance near the subsolar region. It is a considerable deformation relative to Mercury's small magnetosphere. R. M. Winslow et al. (2013) suggested that the subsolar standoff distance of the magnetopause varies by $0.2 R_M$ in response to a solar wind dynamic pressure change of 12.8 nPa. The deformation of the magnetopause caused by jets is comparable to the variation in magnetopause standoff distance caused by the solar wind dynamic pressure change.

4. Conclusions and Discussion

In this study, we explore whether magnetosheath jets can form at Mercury by performing a 3D global hybrid simulation. The simulation results show that the magnetosheath jets can result from upstream CSs passing through the shock surface. The parallel size of magnetosheath jets can reach $0.53 R_M$, which is significantly smaller than that at Earth, where their parallel size can reach several R_E . Previous studies suggested that magnetosheath jets are cylinder like or pancake like (see F. Plaschke et al. 2018, and references therein). However, our simulation demonstrates that the 3D magnetosheath jets surround the quasi-circular magnetosheath cavities where the dynamic pressure decreases, just like rings. The diameter of

magnetosheath cavities can reach $1 R_M$. Honeycomb-like magnetosheath structures, which are combinations of magnetosheath jets and cavities at Earth, cannot form at Mercury due to its small magnetosphere size. We also investigate the properties of magnetosheath jets and cavities using virtual stationary spacecraft. When a virtual spacecraft is located in a jets-dominated region, five jets are observed within 90 s; when a virtual spacecraft is located in a cavities-dominated region, only one jet is observed. Moreover, the magnetopause is deformed by the magnetosheath jets and cavities, with deformation reaching up to $0.19 R_M$. Magnetosheath jets, as pressure pulses, can lead to the formation of traveling compression regions (M. B. Moldwin et al. 2001) around the magnetopause deformation, which may modulate and energize ion in the ring current. We infer that the jets and cavities in Mercury's magnetosheath may have a significant impact on the planetary magnetosphere dynamics.

Acknowledgments

This research was funded by the Strategic Priority Research Program of Chinese Academy of Sciences grant No. XDB41000000; the National Science Foundation of China (NSFC) grant 42174181, 42274196 and 42241160; and ISSI-BJ International Team "Interaction between magnetic reconnection and turbulence: From the Sun to the Earth." Computer resources were provided by the Hefei Advanced Computing Center of China. The authors gratefully acknowledge the data resources from the "National Space Science Data Center, National Science & Technology Infrastructure of China (<http://www.nssdc.ac.cn>)." Plasma data (such as ion density, ion velocity, and ion temperature, etc.) and magnetic field data used to plot all figures in this study can be downloaded from 10.57760/sciencedb.space.01492.

ORCID iDs

Jin Guo  <https://orcid.org/0000-0002-9950-1029>
 San Lu  <https://orcid.org/0000-0003-2248-5072>
 Quanming Lu  <https://orcid.org/0000-0003-3041-2682>
 Junyi Ren  <https://orcid.org/0000-0002-0173-5290>
 Jiuqi Ma  <https://orcid.org/0000-0001-5665-3957>
 James A. Slavin  <https://orcid.org/0000-0002-9206-724X>
 Weijie Sun  <https://orcid.org/0000-0001-5260-658X>
 Jun Zhong  <https://orcid.org/0000-0003-4187-3361>
 Xinliang Gao  <https://orcid.org/0000-0003-0767-2267>
 Rongsheng Wang  <https://orcid.org/0000-0002-9511-7660>

References

- Anderson, B. J., Johnson, C. L., Korth, H., et al. 2011, *Sci*, 333, 1859
 Archer, M., Hietala, H., Hartinger, M. D., Plaschke, F., & Angelopoulos, V. 2019, *NatCo*, 10, 615
 Archer, M., & Horbury, T. 2013, *AnGeo*, 31, 319
 Dmitriev, A., & Suvorova, A. 2015, *JGRA*, 120, 4423
 Egan, H., Jarvinen, R., Ma, Y., & Brain, D. 2019, *MNRAS*, 488, 2108
 Fatemi, S., Hamrin, M., Krämer, E., et al. 2024, *MNRAS*, 531, 4692
 Fatemi, S., Poppe, A., & Barabash, S. 2020, *JGRA*, 125, e2019JA027706
 Gunell, H., Hamrin, M., Nesbit-Östman, S., Krämer, E., & Nilsson, H. 2023, *SciA*, 9, eadg5703
 Gunell, H., Nilsson, H., Stenberg, G., et al. 2012, *PhPI*, 19, 072906
 Gunell, H., Stenberg Wieser, G., Mella, M., et al. 2014, *AnGeo*, 32, 991
 Guo, J., Lu, S., Lu, Q., et al. 2021a, *JGRA*, 126, e2021JA029388
 Guo, J., Lu, S., Lu, Q., et al. 2021b, *JGRA*, 126, e2020JA028670
 Guo, J., Lu, S., Lu, Q., et al. 2022a, *JGRA*, 127, e2022JA030477
 Guo, J., Lu, S., Lu, Q., et al. 2023a, *JGRE*, 128, e2023JVE008032
 Guo, J., Sun, T., Lu, S., et al. 2023b, *E&PP*, 8, 47

- Guo, J., Wang, B., Lu, S., et al. 2022b, *GeoRL*, 49, e2022GL099753
- Han, D. S., Hietala, H., Chen, X. C., et al. 2017, *JGRA*, 122, 1853
- Hao, Y., Lembège, B., Lu, Q., & Guo, F. 2016, *JGRA*, 121, 2080
- Hietala, H., Laitinen, T. V., Andréová, K., et al. 2009, *PhRvL*, 103, 245001
- Hietala, H., Partamies, N., Laitinen, T., et al. 2012, *AnGeo*, 30, 33
- Hietala, H., Phan, T., Angelopoulos, V., et al. 2018, *GeoRL*, 45, 1732
- Hietala, H., Trotta, D., Fedeli, A., et al. 2024, *MNRAS*, 531, 2415
- Jia, X., Slavin, J. A., Poh, G., et al. 2019, *JGRA*, 124, 229
- Karimabadi, H., Roytershteyn, V., Vu, H. X., et al. 2014, *PhPI*, 21, 062308
- Karlsson, T., Kullen, A., Liljeblad, E., et al. 2015, *JGRA*, 120, 7390
- Karlsson, T., Liljeblad, E., Kullen, A., et al. 2016, *P&SS*, 129, 61
- Katircioğlu, F., Kaymaz, Z., Sibeck, D., & Dandouras, I. 2009, *AnGeo*, 27, 3765
- Lapenta, G., Schriver, D., Walker, R. J., et al. 2022, *JGRA*, 127, e2021JA030241
- Li, C., Jia, X., Chen, Y., et al. 2024, *JGRA*, 129, e2024JA032669
- Lu, Q., Guo, J., Lu, S., et al. 2022, *ApJ*, 937, 1
- Lu, Q., Ke, Y., Wang, X., et al. 2019, *JGRA*, 124, 4157
- Marsch, E., Mühlhäuser, K. H., Schwenn, R., et al. 1982, *JGR*, 87, 52
- Moldwin, M. B., Collier, M. R., Slavin, J. A., & Szabo, A. 2001, *GeoRL*, 28, 1925
- Němeček, Z., Šafránková, J., Přeč, L., et al. 1998, *GeoRL*, 25, 1273
- Omelchenko, Y., Chen, L. J., & Ng, J. 2021, *JGRA*, 126, e2020JA029035
- Omidi, N., Berchem, J., Sibeck, D., & Zhang, H. 2016, *JGR*, 121, 3155
- Palmroth, M., Hietala, H., Plaschke, F., et al. 2018, *AnGeo*, 36, 1171
- Plaschke, F., Glassmeier, K.-H., Sibeck, D., et al. 2009, *AnGeo*, 27, 4521
- Plaschke, F., Hietala, H., & Angelopoulos, V. 2013, *AnGeo*, 31, 1877
- Plaschke, F., Hietala, H., Archer, M., et al. 2018, *SSRv*, 214, 81
- Plaschke, F., Hietala, H., & Vörös, Z. 2020, *JGRA*, 125, e2020JA027962
- Plaschke, F., Karlsson, T., Hietala, H., et al. 2017, *JGRA*, 122, 10
- Raptis, S., Karlsson, T., Plaschke, F., Kullen, A., & Lindqvist, P.-A. 2020, *JGRA*, 125, e2019JA027754
- Raptis, S., Karlsson, T., Vaivads, A., et al. 2022, *NatCo*, 13, 598
- Ren, J., Guo, J., Lu, Q., et al. 2024, *GeoRL*, 51, e2024GL109925
- Ren, J., Lu, Q., Guo, J., et al. 2023, *JGRA*, 128, e2023JA031699
- Romanelli, N., & DiBraccio, G. 2021, *NatCo*, 12, 6748
- Romanelli, N., DiBraccio, G., Gershman, D., et al. 2020, *GeoRL*, 47, e2020GL087350
- Russell, C., Hoppe, M., & Livesey, W. 1982, *Natur*, 296, 45
- Sarantos, M., & Slavin, J. A. 2009, *GeoRL*, 36, L04107
- Shi, Z., Rong, Z., Fatemi, S., et al. 2022, *GeoRL*, 49, e2022GL098415
- Shue, J. H., Chao, J. K., Song, P., et al. 2009, *GeoRL*, 36, L18112
- Slavin, J., Middleton, H., Raines, J., et al. 2019, *JGRA*, 124, 6613
- Slavin, J. A., Acuña, M. H., Anderson, B. J., et al. 2008, *Sci*, 321, 85
- Slavin, J. A., & Holzer, R. E. 1981, *JGR*, 86, 11401
- Sun, W., Dewey, R. M., Aizawa, S., et al. 2022, *ScChD*, 65, 25
- Sundberg, T., Boardsen, S. A., Burgess, D., & Slavin, J. A. 2015, *JGRA*, 120, 7342
- Sundberg, T., Boardsen, S. A., Slavin, J. A., et al. 2013, *JGRA*, 118, 6457
- Suni, J., Palmroth, M., Turc, L., et al. 2021, *GeoRL*, 48, e2021GL095655
- Wang, Y., Zhong, J., Slavin, J., et al. 2023, *GeoRL*, 50, e2022GL102574
- Winslow, R. M., Anderson, B. J., Johnson, C. L., et al. 2013, *JGRA*, 118, 2213
- Zhong, J., Wei, Y., Lee, L., et al. 2020, *ApJL*, 893, L18
- Zhou, Y., Raptis, S., Wang, S., et al. 2024, *NatCo*, 15, 4